



Surface water $f\text{CO}_2$ algorithms for the high-latitude Pacific sector of the Southern Ocean

Melissa Chierici ^{a,*}, Sergio R. Signorini ^{b,c}, My Mattsdotter-Björk ^a, Agneta Fransson ^{d,1}, Are Olsen ^{e,f}

^a Department of Chemistry, University of Gothenburg, SE-412 96 Göteborg, Sweden

^b Science Applications International Corporation, Beltsville, Maryland, USA

^c NASA Goddard Space Flight Center, Greenbelt, Maryland, USA

^d Department of Earth Sciences, University of Gothenburg, SE-405 30 Göteborg, Sweden

^e Uni Bjerknnes Centre, Allégaten 55, N-5007 Bergen, Norway

^f Bjerknnes Centre for Climate Research, Allégaten 55, N-5007 Bergen, Norway

ARTICLE INFO

Article history:

Received 22 October 2010

Received in revised form 29 November 2011

Accepted 22 December 2011

Available online xxxx

Keywords:

Seasonal ice zone

Oceanic CO_2 uptake

Seasonal variability

Validation of satellite data

Biological CO_2 drawdown

Western Antarctica

Polar Oceans

ABSTRACT

The feasibility of using remotely sensed data jointly with shipboard measurements to estimate the carbon dioxide fugacity in the surface water ($f\text{CO}_{2\text{sw}}$) of the Pacific sector of the Southern Polar Ocean ($S > 60^\circ\text{S}$) is evaluated using a data set obtained during austral summer 2006. A comparison between remotely sensed chlorophyll a (chl a) and sea-surface temperature (SST) with in-situ measurements, reveals the largest bias in areas with rapid and large concentration changes such as at the ice edge, the polar front and in the Ross Sea Polynya. The correlation between $f\text{CO}_{2\text{sw}}$ and SST, chl a, biological productivity estimates and mixed layer depth (MLD) are evaluated, and single and multiple regression methods are used to develop $f\text{CO}_{2\text{sw}}$ algorithms. Single regressions between the study parameters and $f\text{CO}_{2\text{sw}}$ show that most of the $f\text{CO}_{2\text{sw}}$ variability is explained by chl a. The Multi-Parameter Linear regressions were used to create $f\text{CO}_{2\text{sw}}$ algorithms derived from field measurements, and using solely remote-sensing products. Based on the best fits from the two data sets $f\text{CO}_{2\text{sw}}$ estimates have a root means square deviation of $\pm 14 \mu\text{atm}$ and coefficient of determination of 0.82. The addition of satellite derived estimates of biological productivity in the algorithm does not significantly improve the fit. We use the algorithm with remotely sensed chl a and SST data to produce an $f\text{CO}_{2\text{sw}}$ map for the entire high-latitude Southern Ocean south of 55°S . We analyze and discuss the seasonal and spatial robustness of the algorithm based on the remotely sensed data and compare with climatologic $f\text{CO}_{2\text{sw}}$ data.

© 2012 Elsevier Inc. All rights reserved.

1. Introduction

The global oceans act as buffers for carbon dioxide (CO_2) with an annual uptake corresponding to approximately one-quarter of the anthropogenic emissions (Takahashi et al., 2009). The Southern Ocean is, in particular, recognized as one of the most important regions for the global marine carbon cycle. The response of the Southern Ocean to climate change such as global warming and increased wind induced upwelling of CO_2 -rich subsurface waters are predicted to have a large impact on the global oceanic CO_2 uptake (Le Quéré et al., 2007; Sarmiento et al., 1998). The large CO_2 uptake of this region is due to its sheer size coupled with strong heat loss, as well as strong winds and rough seas that favor air–sea CO_2 gas exchange (Robertson & Watson, 1995; Takahashi et al., 2009). At present, the Southern Ocean is generally considered to be a net sink for atmospheric CO_2 (Bakker et al., 1997; Hoppema et al., 2000; Metzl, 2009; Robertson & Watson, 1995;

Takahashi et al., 2009). In the confluence between the warmer subtropical waters and the sub-Antarctic waters, a strong CO_2 -sink zone has been observed between 40°S and 55°S (e.g. Barbero et al., 2011; Chierici et al., 2004; Inoue-Yoshikawa & Ishii, 2005; McNeil et al., 2007; Metzl, 2009; Metzl et al., 1999; Poisson et al., 1993; Takahashi et al., 1993), likely due to the effect of the strong cooling of warm subtropical waters and the resulting increase of CO_2 solubility. However, the magnitude of this sink, and in particular its degree of inter-annual variability, are not well known (e.g. Takahashi et al., 2009). The challenges to estimate oceanic CO_2 uptake trends from observations are also seen in the long-term data set (1969 to 2002) in the area south of Australia, where no trend could be estimated due to a large bloom in January (Inoue-Yoshikawa & Ishii, 2005). In the seasonally sea-ice covered areas ($> 60^\circ\text{S}$), rapid biological CO_2 uptake, during and upon ice melt, offsets the winter time CO_2 supersaturation, and creates a summertime CO_2 sink in the Weddell Sea gyre (Bakker et al., 2008). The fugacity of carbon dioxide in the surface water ($f\text{CO}_{2\text{sw}}$) of large areas of the Southern Ocean, in particular the high-latitude polar ($> 60^\circ\text{S}$) waters in the Pacific sector, are still largely unknown (Fig. 1). Even in the relatively well studied Ross Sea, Arrigo and van Dijken (2007) point out the few air–sea CO_2

* Corresponding author. Tel.: +46 317869114.

E-mail address: melissa@chem.gu.se (M. Chierici).

¹ Now at: Norwegian Polar Institute, Fram Centre, NO-9296, Tromsø, Norway.

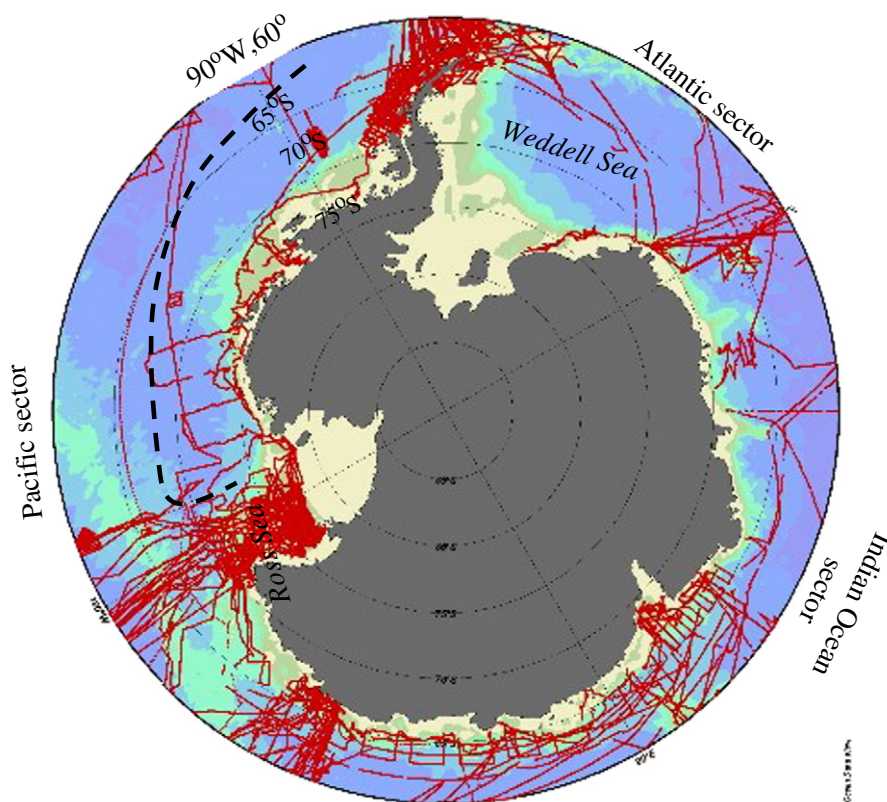


Fig. 1. Summary of the former expeditions (red lines) of underway $f\text{CO}_2\text{sw}$ measurements that have been performed in the circumpolar Southern Ocean south of 60°S between 1970 and 2005, based on the Surface Ocean CO_2 Atlas (SOCAT, www.socat.info). The IB Oden cruise track for 2006 is shown as the black line. (For interpretation of the references to color in this figure legend, the reader is referred to the web version of this article.)

flux estimates. These values show that the Ross Sea acts as a CO_2 sink, mainly due to biological CO_2 drawdown during photosynthesis (Sweeney et al., 2000). Consequently, estimates of the net mean annual sea–air CO_2 flux in the high-latitude Southern Ocean ($> 60^\circ\text{S}$) are few and have low spatial coverage (Chierici et al., 2004; McNeil et al., 2007; Takahashi et al., 2009). To overcome this, methods for mapping scattered $f\text{CO}_2\text{sw}$ data must be devised. The use of Multi-Parameter Linear Regression (MLR) equations are one such approach that have been developed over the last decade. This approach takes advantage of empirical relationships that exist between $f\text{CO}_2\text{sw}$ and remotely sensed mapped variables (sea surface temperature and chlorophyll a in many regions), to generate maps of $f\text{CO}_2\text{sw}$. Its application areas include, for instance, the Pacific (Boutin et al., 1999; Rangama et al., 2005; Stephens et al., 1995) and the Caribbean Sea (Olsen et al., 2004). Recently Mixed Layer Depth (MLD) derived from Ocean reanalysis models was introduced as another promising $f\text{CO}_2\text{sw}$ proxy by Olsen et al. (2008), and its potential was further enlightened by Chierici et al. (2009) and Telzewski et al. (2009). For complete ocean coverage there is a strong need to explore the development of algorithms in other oceanic regions as well.

Relationships of $f\text{CO}_2\text{sw}$ to sea surface temperature (SST) and chlorophyll a (chl a) in the region between 45°S and 60°S south of Tasmania and New Zealand were developed and used to create $f\text{CO}_2\text{sw}$ fields by Rangama et al. (2005). They used linear regressions between $f\text{CO}_2\text{sw}$ and either SST or chl a, and estimated $f\text{CO}_2\text{sw}$ with the accuracy of approximately $10 \mu\text{atm}$. The present paper explores the feasibility of developing $f\text{CO}_2\text{sw}$ algorithms even further south, ($> 60^\circ\text{S}$) in the seasonally ice covered Pacific sector of the Southern Ocean. The region is to a large extent unexplored due to harsh sampling conditions and the need for icebreakers. Satellite sensors have superior spatial and temporal resolution, and it is of great interest to use remotely sensed data to produce algorithms to estimate $f\text{CO}_2\text{sw}$ in the surface water in this climatically sensitive region. This

is a first attempt to systematically evaluate the ability of several parameters (namely chl a, SST, and MLD) acting as proxies for $f\text{CO}_2\text{sw}$ in this region, both on their own and combined in MLR equations. For this purpose, we include the assessment of the applicability of satellite derived primary productivity. We also compare field data and remotely sensed products.

2. Study area

Our study area covers part of the region between Punta Arenas, Chile and the McMurdo station, at the coast of Ross Sea, Antarctica, which was traversed by the *IB Oden* between the 12th and 26th of December 2006 (dashed line in Fig. 1). Fig. 2a to d show remotely sensed SST (SST^{rmt} , Sect. 3.3), salinity (SSS) and MLD from the Hybrid Coordinate Ocean Model, HYCOM, (Sect. 3.2), and remotely sensed chl a (chl^{rmt} , Sect. 3.3), and the black line represents the underway sampling locations onboard the *IB Oden*. The ship ventured through both ice-covered areas (sea-ice zone, SIZ) and the permanently open ocean zone (POOZ, Fig. 2). The approximate extent of the sea-ice cover in winter (winter ice edge) is shown as the dashed white line in Fig. 2. Strong salinity and temperature gradients were defined as fronts according to previous protocols (Orsi & Whitworth, 2005; Orsi et al., 1995). Frontal systems, such as the sub-Antarctic Front (SAF), the Antarctic Polar Front (APF), as well as the ice edge in the Southern Ocean are strongly associated with high primary production (e.g. Moore & Abbott, 2000, Fig. 2d). POOZ denotes the area with no seasonal sea-ice cover, which is located north of the Sea Ice Zone (SIZ). SIZ is defined as the region between the summertime minimum and wintertime maximum sea-ice extent. Large seasonal changes occur in the sea-ice cover from summer to winter (Arrigo et al., 1998). The SAF marks the northern frontier of the Antarctic Circumpolar Current (ACC), where warm and salty subtropical surface

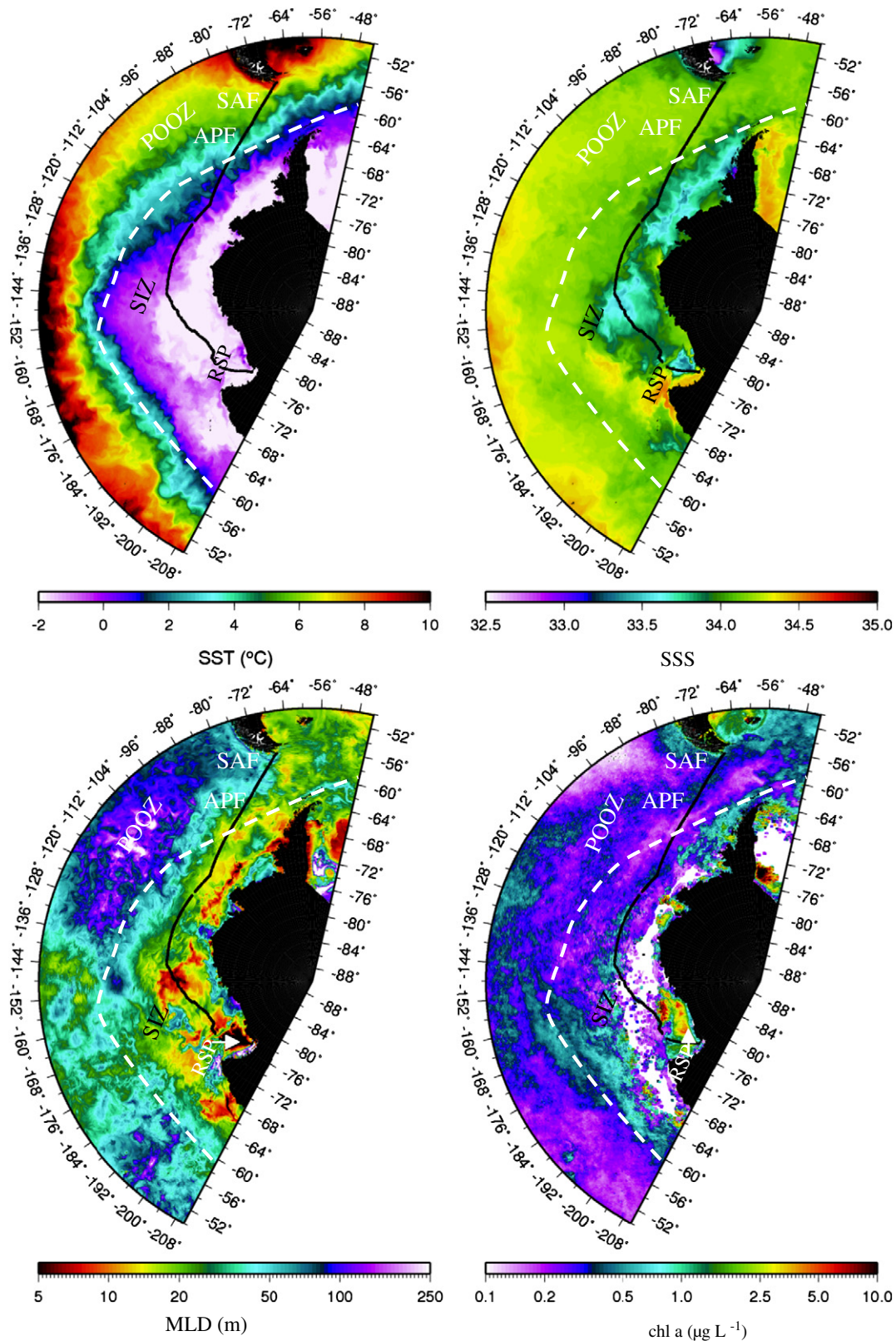


Fig. 2. The extension and variability of the a) remotely sensed sea surface temperature, SST, ($^{\circ}\text{C}$), b) sea surface salinity (SSS), c) the modeled mixed layer depth, MLD (m), and the d) remotely sensed chlorophyll a (chl, $\mu\text{g L}^{-1}$) along the cruise track (black line) in large parts of the Pacific sector of the Southern Ocean from $\sim 50^{\circ}\text{S}$ to 80°S . The HYCOM products SSS and MLD are from December 2006 and the remotely sensed chl image is December climatology (1997–2008) to avoid cloud masking of the entire region. The major fronts and zones are marked and are denoted as follows; the Permanently Open Ocean Zone (POOZ), Subantarctic Front (SAF), Antarctic Polar Front (APF), the Sea Ice Zone (SIZ). The Ross Sea Polynya is denoted RSP. The white dashed line shows the approximate location of the winter ice edge (August).

water mixes with cold and fresher sub-Antarctic water, and is generally defined as the location where the temperature decreases southwards from 9 °C to 5 °C. The Ross Sea Polynya (RSP) is the largest polynya in Antarctica, approximately 105 km² (Arrigo & van Dijken, 2003). The RSP is formed by upwelling of warm modified circumpolar deep water (CDW) that reduces the ice formation during the winter in combination with catabatic winds (which form over the inland glaciers) that move newly formed ice to the north and away from the fixed ice edge or the coastline (Arrigo & Van Dijken, 2007). These winds together with currents help to maintain the polynya open during the summer.

2.1. In-situ observations

Based on the SST from this study and the definitions by Orsi et al. (1995), we found the SAF to be located between 56° and 58°S (Figs. 2 and 3). Here, we observed cooling from 8 °C to 5 °C. The northern boundary of the Antarctic Front (APF) was found at ~63°S, which is marked by a sharp temperature gradient from 4.1 °C to 1.2 °C. At approximately 65°S and 66°S, we observed two chl *a* peaks coinciding with drastic *f*CO_{2sw} decrease and rapid cooling from 2 °C to -0.1 °C, as we entered the Antarctic Zone (AZ). This implied enhanced biological production associated with the APF, which has been reported

previously (e.g. Arrigo et al., 1998; Chierici et al., 2004). In the AZ, the ice edge was reached at 67.5°S, 102°W. In the SIZ, the salinity varied (from 33.65 to 34.00) and SST was just above the freezing point (-1.1 to -1.7°C). Entering the RSP, both salinity and SST increased remarkably to 34.3 and 0.5 °C, respectively. The mean extent of the sea-ice cover in December 2006 with the overlay of cruise track and daily mean location of the ship is shown in Fig. 4. For more detailed description of the sea-ice conditions, we refer to the study by Ozsoy-Cicek et al. (2008). The ship stayed mainly in the POOZ or in the SIZ, and spent only a few days in heavy sea-ice conditions before the opening of the RSP.

3. Data

3.1. Field data

Seawater for underway measurements was drawn from a water intake placed at the depth of approximately eight meters at the bow of *IB Oden*. The water was pumped through stainless steel tubing to the instruments, and on-line measurements were made every minute for surface water fugacity of CO₂ (*f*CO_{2sw}), chl *a* fluorescence (chl *a*^{fluor}), SST and SSS.

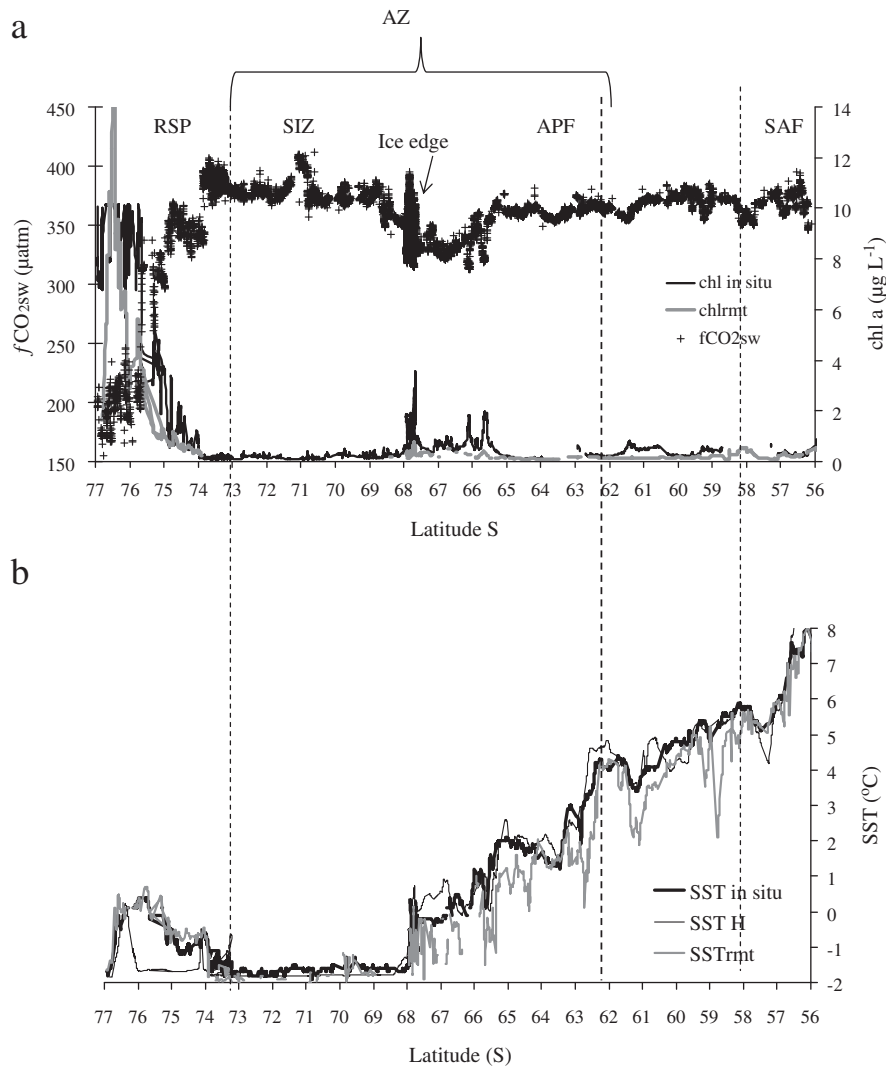


Fig. 3. The latitudinal variability of: a) *f*CO_{2sw} (μatm, black cross), in situ chlorophyll *a* (black line), chl^{insitu} (μg L⁻¹) and satellite chl, (chl^{mt} gray line, μg L⁻¹), b) in situ SST (black thick line, °C), HYCOM SST (SST^H, thin black line, °C) and satellite SST (SST^{mt}, gray line, °C). Major fronts and zones are marked with dashed vertical lines. The northern boundary of the Antarctic Front (APF) is found at ~63°S. The arrow shows the approximate location of the ice edge. Note that the furthest south is to the left at the axis.

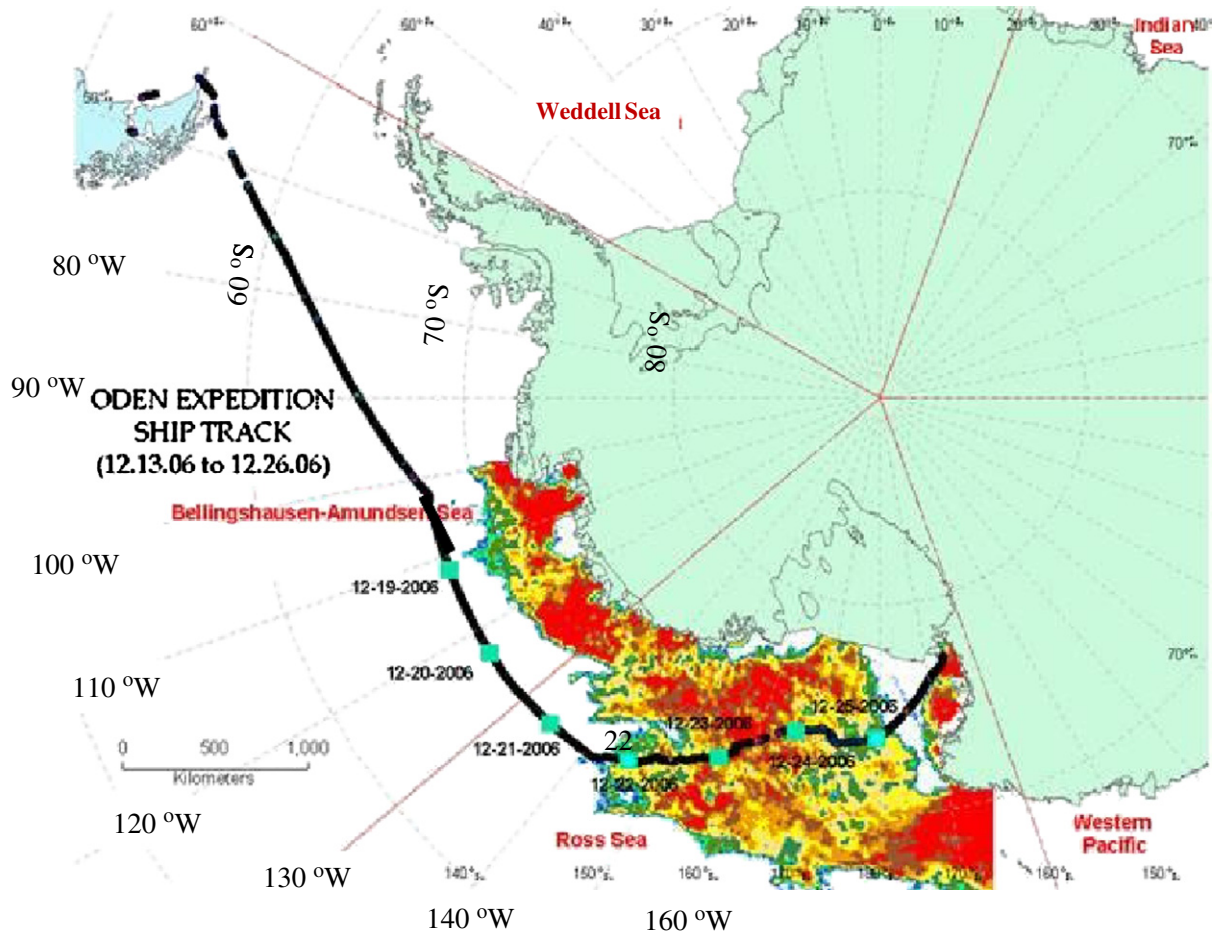


Fig. 4. The sea-ice concentration and extent along the cruise track of IB Oden in December 2006. The red, yellow, and green colors denote 90 to 100%, 50% and 30% ice coverage, respectively. The dates (MM-DD-2006) are shown for each station location along the cruise track. Courtesy: Burcu Ozsoy-Cicek, University of San Antonio, Texas, USA. (For interpretation of the references to color in this figure legend, the reader is referred to the web version of this article.)

3.1.1. Fugacity of carbon dioxide in the surface water

For the continuous $f\text{CO}_2\text{sw}$ measurements, seawater was pumped at the flow rate of approximately 15 L min^{-1} into a CO_2 equilibrator (tandem type combined with a static mixer type manufactured by Kimoto Electric Co., LTD (Harashima et al., 1997; Kimoto & Harashima, 1993)). Prior to analysis, the air was treated and dried in several steps, which included aerosol filters, a Peltier cooling element, and Nafion tubing. Raw voltage readings of the non-dispersive infrared detector (NDIR, LiCOR®, model 6262, Lincoln, USA) were continuously measured every 10 s and converted to the mole fraction of CO_2 in dry air ($x\text{CO}_2$, ppm) using four CO_2 standard gasses and zero gas (0, 250, 350, 450, 550 ppm, supplied by Strandmøllen, Denmark) used for calibration every 12th hour. These gas calibration standards were used for the accurate characterization of the non-linear response curve from the NDIR detector to changing CO_2 concentrations (Dickson et al., 2007). The accuracy of the CO_2 -gas standards was between 0.5% (for the 250 and 350 ppm concentrations) and 1% (450 and 550 ppm). The $x\text{CO}_2$ in dry air was converted to $f\text{CO}_2$ in moist air (in the equilibrator) using temperature, salinity and pressure in the equilibrator as described by Weiss and Price (1980). Subsequently, the $f\text{CO}_2$ of moist air at sea surface conditions ($f\text{CO}_2\text{sw}$, μatm) was estimated from the in-situ temperature in the surface water (SST), salinity, and air pressure (Beer, 1983; Weiss et al., 1982). The $f\text{CO}_2\text{sw}$ data varied between 165 and 412 μatm and showed rapid changes at the APF, the ice edge and in the Ross Sea (Fig. 3a).

In addition to underway $f\text{CO}_2\text{sw}$ measurements, we collected discrete surface samples at 37 locations for the measurements of total alkalinity

(A_T) and total inorganic carbon (C_T). All A_T and C_T samples were analyzed onboard the ship. A_T was determined by potentiometric titration in an open cell with 0.05 M HCl, according to Haraldsson et al. (1997). C_T was analyzed by coulometric titration. Analytical methods for the A_T and C_T determinations have fully been described in more detail elsewhere [i.e. Dickson et al., 2007]. The precision was computed from three replicate analyses of one sample at least twice daily and was determined to $\pm 2 \mu\text{mol kg}^{-1}$ ($\pm 0.1\%$). Routine analyses of Certified Reference Materials (CRM, provided by A. G. Dickson, Scripps Institution of Oceanography) ensured the accuracy of the measurements, which was better than $\pm 1 \mu\text{mol kg}^{-1}$ and $\pm 2 \mu\text{mol kg}^{-1}$ for C_T and A_T , respectively.

Total alkalinity, C_T , salinity and temperature were used as input parameters in a CO_2 -chemical speciation model (CO2SYS program, Pierrot et al., 2006) to calculate $f\text{CO}_2$ ($f\text{CO}_2\text{sw}^{\text{calc}}$). This allowed an internal consistency check of the underway $f\text{CO}_2\text{sw}$. We used the CO_2 -system dissociation constants (K^*1 and K^*2) estimated by Roy et al. (1993, 1994), since a previous study showed these constants to be the most suitable constants for cold and fresher surface waters (Chierici & Fransson, 2009). The calculations were performed on the total hydrogen ion scale, and we used the HSO_4^- dissociation constant of Dickson (1990). The linear regression between the measured underway $f\text{CO}_2\text{sw}$ data and the calculated data ($f\text{CO}_2\text{sw}^{\text{calc}} = 0.972x f\text{CO}_2\text{sw}$, $N = 37$, zero-intercept) resulted in a coefficient of determination (r^2) of 0.999, and a root mean square error (rms) of $\pm 9 \mu\text{atm}$. Thus, the error in $f\text{CO}_2\text{sw}$ of $\pm 9 \mu\text{atm}$ was considered the lower limit of the expected error in further calculations.

3.1.2. Sea surface temperature and salinity

SST (Fig. 3b) and SSS (not shown) were continuously measured using a thermosalinograph SBE-21 (Seabird Electronics Inc.). The accuracy and precision for SST and SSS were ± 0.01 °C and ± 0.001 , respectively. Another temperature sensor was located at the seawater intake, upstream of the pump, for the accurate temperature measurements of incoming water (SST). The temperature difference between the equilibrator and the seawater intake was 0.65 ± 0.09 °C, which was corrected for in the $f\text{CO}_{2\text{sw}}$ calculation (see 3.1.1).

3.1.3. Chlorophyll a

High frequency measurements of $\text{chl}^{\text{fluor}}$ were obtained with a chl a fluorescence sensor installed in a flow-through manifold (MiniTracka II, Chelsea Technologies Group). The MiniTracka II used an excitation wavelength centered at 470 nm and the bandwidth of 30 nm, and an emission wavelength centered at 685 nm and at 30 nm bandwidth. The accuracy of the MiniTracka II is $\pm 0.02 \mu\text{g L}^{-1}$. Seawater was pumped through the manifold at the speed of 1 L min^{-1} and voltage data were recorded every 10 s, which were averaged to 1-minute data. The MiniTracka II was calibrated against the total of 35 chl a measurements (chl^{extr}) obtained from discrete samples, which were collected and analyzed after extraction using the acetone-spectrofluorometric method (Holm-Hansen & Riemann, 1978). The linear correlation between the MiniTracka II sensor fluorescence voltage (V^{fluor}) and the extracted chl a, $\text{chl}^{\text{extr}} = 1.9854 \times V^{\text{fluor}} - 0.1013$ ($r^2 = 0.902$, $N = 35$) was used to convert the voltage signal to in-situ chl a ($\text{chl}^{\text{in situ}}$, Fig. 3a).

3.2. Ocean analysis data

The HYCOM + NCODA (HYbrid Coordinate Ocean Model + NRL Coupled Ocean Data Assimilation) system is a data-assimilative hybrid isopycnal-sigma-pressure (generalized) coordinate ocean model system that uses satellite sea-surface height, in-situ salinity and temperature data from numerous sources (e.g. the Argo buoy program, PIRATA moorings) to provide reconstructions of the ocean state such as MLD (Hurlburt et al., 2009). We extracted the daily 1/12 degree SST, SSS and MLD products from the HYCOM + NCODA global hind cast analysis (from November 2003 to present) from the nearest points within 0.05° of longitude and 0.1° of latitude, and averaged within that distance. The data were obtained from http://tds.hycom.org/thredds/global_combined/glb_analysis_catalog.html?dataset=GLBa0.08/glb_analysis. The HYCOM SST data are evaluated along with the satellite SST product in Section 3.3.

The HYCOM MLD (MLD_H) product was compared with mixed layer depth estimates derived from temperature profiles from Expendable Bathythermographs (XBT), deployed at 47 locations between 68°S and 74°S . The MLD from XBT's (MLD_{XBT}) was defined as the depth where the temperature differed by 0.2 °C from the surface temperature (upper 5 m) according to Lorbacher et al. (2006). The MLD_H was shallower than the MLD_{XBT} (Fig. 5) by about 7 m. The r^2 from a linear fit was 0.69 and rms was ± 10 m.

3.3. Remotely sensed chl a and SST

We used the 8-Day Level 3 merged SeaWiFS/MODIS chl a product created and distributed by the Ocean Biology Processing Group (OBPG, <http://oceancolor.gsfc.nasa.gov>) using the satellite measurements from Moderate Resolution Imaging Spectroradiometer, MODIS, (OC3M algorithm), in orbit on the Aqua satellite, and the Sea-viewing Wide Field-of-view Sensor (SeaWiFS, OC4V4 algorithm), in orbit on the OrbView-2 platform. This product has increased coverage over the single mission products, which is important for high-latitude regions. For SST, we used the mapped 8-Day product from MODIS, which has a resolution of 9 km.

The satellite data were collocated with the $f\text{CO}_{2\text{sw}}$ data (Fig. 3a) obtained from the *IB Oden* expedition with the mean distance

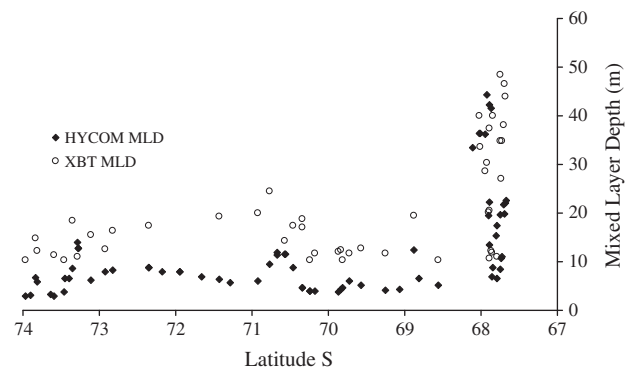


Fig. 5. The latitudinal variability of Mixed Layer Depth (MLD, meters) derived from the HYCOM model (MLD_H , black diamond), and MLD derived from the in-situ temperature profiles from XBT's (MLD_{XBT} , open rings).

separation of 4.0 km and the standard deviation of ± 5.6 km. Satellite-derived chl a estimates cannot be obtained in the presence of cloudy skies and in completely sea-ice covered regions. Satellite chl a data was not recovered between December 23 and December 25 in 2006, when the ship was in sea ice.

In general terms, the remotely sensed chl a concentrations (chl^{rmt} , $\mu\text{g L}^{-1}$) showed lower values than the in-situ measurements (Figs. 3a and 6a, c). For the whole study area, the mean residual between chl^{rmt} and $\text{chl}^{\text{in situ}}$ showed that chl^{rmt} was lower by $0.19 \mu\text{g L}^{-1}$. The r^2 from a linear fit was 0.86, and the rms was $\pm 1 \mu\text{g L}^{-1}$. Particularly large residuals ($> 1 \mu\text{g L}^{-1}$) were observed at the polar front region, at the ice edge in the area (65 to 68°S , Fig. 6a), and in parts of the RSP. It is clear from this exercise that the satellite chl a product cannot resolve the localized areas of high chl a associated with fronts, and the ice edge, at the spatial and temporal resolutions we were compelled to use to minimize the cloud effects (8 days, 9 km composites). Similar to the chl a product, the SST from HYCOM (SST^H) and remotely sensed (SST^{rmt}) deviated from the SST in situ ($\text{SST}^{\text{in situ}}$). Both SST products had a negative residual median (-0.15 °C, -0.16 °C), meaning that the SST^H and SST^{rmt} were warmer than ship-board SST (Table 1). The linear fit between $\text{SST}^{\text{in situ}}$ and SST^H resulted in r^2 of 0.96 and the rms of ± 0.53 °C. Stronger correlation was found between in-situ SST and SST^{rmt} , and r^2 and the rms were 0.97 and ± 0.43 °C, respectively. As for chl a, the residuals between $\text{SST}^{\text{in situ}}$ and SST^H and SST^{rmt} , were much larger in localized areas where rapid changes occurs, such as fronts, at the ice edge, and in the RSP (Fig. 6b and d). The largest bias in the SST products was found in the RSP, where SST^H was up to 2 °C colder compared to the $\text{SST}^{\text{in situ}}$ (Fig. 6d). This bias would result in 12 μatm to 32 μatm lower predicted $f\text{CO}_{2\text{sw}}$, using the $f\text{CO}_{2\text{sw}}$ and temperature relationship of $0.0423 \text{ }^\circ\text{C}^{-1}$ (Takahashi et al., 1993). This suggests that the predictive capacity of the parameters involved in the algorithms cannot resolve the drastic changes that occur in these localized areas, and that the satellite and model products need to be further developed and optimized with higher resolution.

3.4. Satellite-derived primary productivity

Ocean primary productivity was investigated using a satellite derived Vertically Generalized Production Model (VGPM), which uses a function of chlorophyll a, SST, the daily photoperiod, Photosynthetically Active Radiation (PAR), and euphotic zone depth. We used the hybrid model that employs the basic model structure and parameterization of the standard "Eppley"-curve (Eppley-VGPM) according to Behrenfeld and Falkowski (1997). The Eppley-VGPM differs from the standard VGPM by replacing the polynomial description of Pb_{opt} (physiological variability based on daily integrated production measurements) with the exponential relationship described by Morel

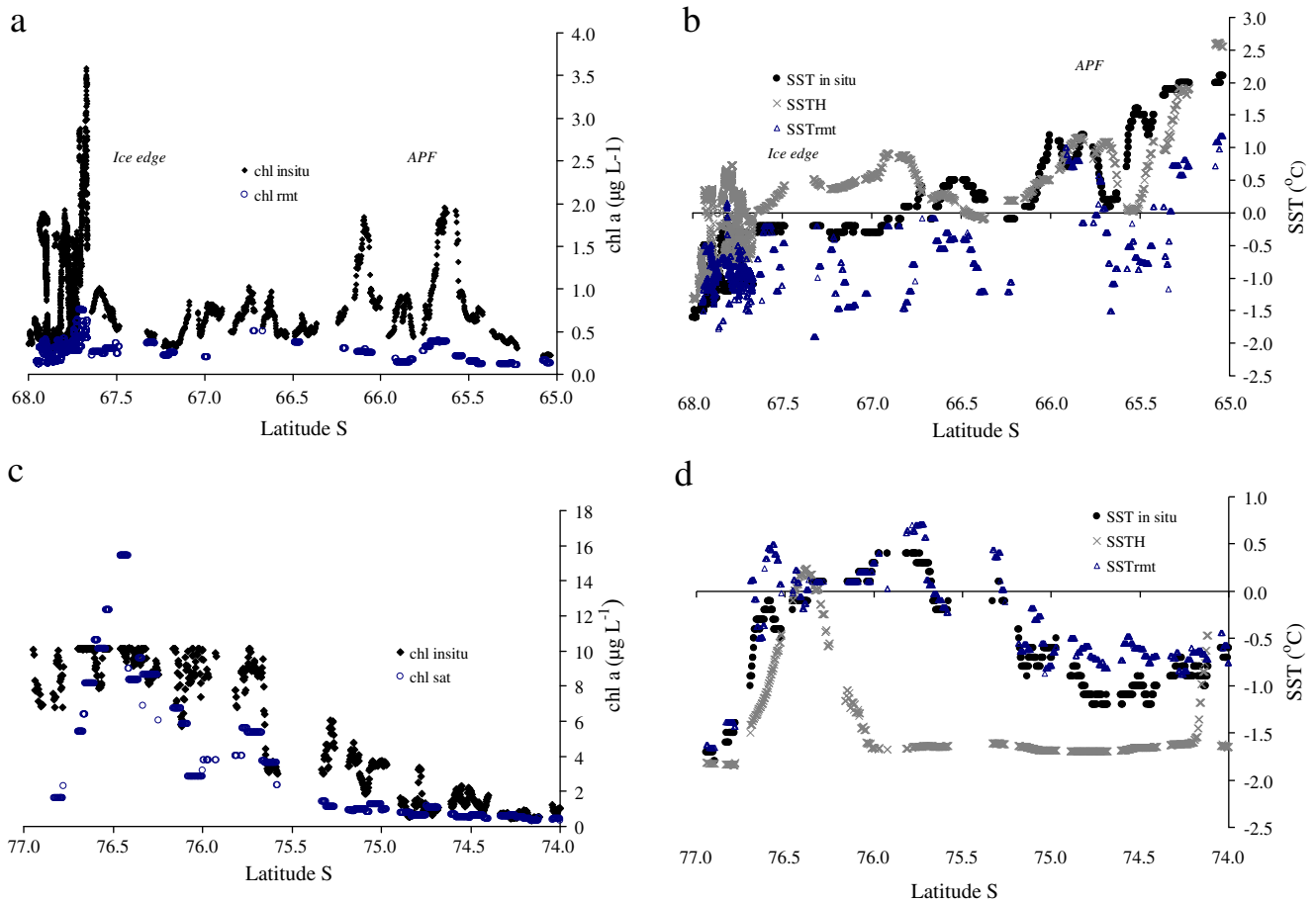


Fig. 6. Chl a ($\mu\text{g L}^{-1}$) and SST ($^{\circ}\text{C}$) are shown in the area between 65°S and 68°S (a, b) and, in the Ross Sea (c, d). The denotations are: chl a $^{\text{in situ}}$ (black), chl $^{\text{rmt}}$ (blue circle), SST $^{\text{in situ}}$ (black dots), SST $^{\text{H}}$ (gray) and SST $^{\text{rmt}}$ (blue). The approximate locations of the polar front (APF) and the ice edge are marked (a,b). Note that the furthest south is to the left at the axis.

(1991). This relationship is based on the curvature of the temperature-dependent growth function described by Eppley (1972). We derived PP $^{\text{sat}}$ estimates using the Eppley-VGPM model (PP $^{\text{satEpp}}$) and satellite-derived products as inputs from 8-Day, 9 km Standard Mapped Image (SMI) SeaWiFS chl a, PAR, and K490 composites and MODIS SST.

4. Evaluation of $f\text{CO}_2\text{sw}$ algorithms

4.1. Single linear regression relationships

To develop algorithms describing the $f\text{CO}_2\text{sw}$ in the surface water, we used proxies that represent the main drivers of $f\text{CO}_2\text{sw}$ variations:

Table 1

Summary of statistics of the comparison between SST $^{\text{in situ}}$ and the remotely sensed SST (SST $^{\text{rmt}}$) and HYCOM SST SST $^{\text{H}}$. The root mean error and the coefficient of determination are denoted rms and r^2 , respectively. A negative mean denotes a warmer SST than the SST $^{\text{in situ}}$ measured onboard the *IB Oden*, and a positive a colder. The 25th percentile value (also referred as the lower quartile) indicates the limit where 25% of the residuals fall below the value in the table. Similarly, the 75th percentile (upper quartile) denotes the value where 75% of the residuals fall below. N denotes the number of data points used in the analysis.

	HYCOM ($^{\circ}\text{C}$)	MODIS ($^{\circ}\text{C}$)
25th percentile	-0.52	-0.39
Median residual	-0.11	-0.18
75th percentile	0.18	0.01
mean	-0.15	-0.16
r^2	0.96	0.97
rms	0.53	0.43
N	10284	10284

temperature, biological processes, and physical mixing. As previously mentioned, the use of chl a and MLD as proxies for $f\text{CO}_2\text{sw}$ in the high-latitude ocean have been investigated for the northern North Atlantic, which showed great potential (Chierici et al., 2009; Olsen et al., 2008). In the present paper, we explored algorithms to compute $f\text{CO}_2\text{sw}$ in the high-latitude Pacific sector of the Southern Ocean, using SST (in situ and remotely sensed), chl a (in situ and remotely sensed), MLD (HYCOM model), and PP $^{\text{satEpp}}$. Single linear regressions between $f\text{CO}_2\text{sw}$ and proxy parameters were used to identify suitable predictors for $f\text{CO}_2\text{sw}$. These are included in Multi-Parameter Linear Regression relationships based on the Marquardt Levenberg routine (Press et al., 1986), implemented in the STATISTICA software. The range of the $f\text{CO}_2\text{sw}$ and the independent variables chl a, SST, MLD, and PP $^{\text{satEpp}}$ (NB: PP $^{\text{satEpp}}$ is dependent of chl a) are summarized in Table 2.

In order to obtain the fundamental understanding of the relationship between $f\text{CO}_2\text{sw}$ and its potential predictors, single linear regression analyses were carried out according to the schematic equation: $f\text{CO}_2\text{sw} = kx + m$, where x denotes the potential predictor variable and k is the slope and m is the intercept. The independent variables (predictors) are SST $^{\text{in situ}}$, chl a $^{\text{in situ}}$, PP $^{\text{satEpp}}$ and MLD. For some of the parameters, we also investigated the performance of the quadratic (SST $^{\text{in situ}}$) and logarithm (chl a $^{\text{in situ}}$ and MLD) of the predictor variable since such functional relationships have been identified elsewhere (Chierici et al., 2009; Olsen et al., 2008). However, the logarithm function of SST $^{\text{in situ}}$ can only be performed on SST > 0 and was not applicable in this study. The exponential function of SST $^{\text{in situ}}$ showed less predictable power than the quadratic function. The results from the single regression analysis are summarized in Table 3. The performance

Table 2

The range of the $f\text{CO}_2\text{sw}$ and the independent variables $\text{SST}^{\text{in situ}}$, $\text{chl a}^{\text{in situ}}$, MLD^{H} , and $\text{PP}^{\text{satEpp}}$.

	$f\text{CO}_2^{\text{sw}}$ (μatm)	$\text{SST}^{\text{in situ}}$ ($^{\circ}\text{C}$)	$\text{chl a}^{\text{in situ}}$ ($\mu\text{g L}^{-1}$)	MLD^{H} (m)	$\text{PP}^{\text{satEpp}}$ ($\text{mg C m}^{-2} \text{d}^{-1}$)
Minimum value	165	−1.90	0.08	3	148
Maximum value	412	7.60	10.16	152	2368
Mean	355	0.52	0.87	16	310
Standard deviation	± 32	± 2.50	± 1.64	± 16	± 285

□ This study using Eppley-VGPM model based on calculation described in Section 3.4.

of the fit was assessed statistically and evaluated from criteria recommended by Allen et al. (2007), which has been used to evaluate the quality on oceanic CO_2 system data sets (Nondal et al., 2009). For the assessment, we used: 1) the r^2 , which is the measure of the percentage of the variability in the in-situ measurements that can be accounted for by the fit (e.g. Allen et al. 2007), 2) the rms of the fit, and 3) the normalized regression coefficients (β) as indicators for the predictive capacity of MLD, SST, chl a, and $\text{PP}^{\text{satEpp}}$ to estimate $f\text{CO}_2\text{sw}$. The β coefficients are the regression coefficients when all variables are standardized to the mean value of 0 and standard deviation of 1. All variables were standardized by subtracting the mean and dividing by the standard deviation. Thus the β coefficients allowed for the direct comparison of the relative contribution of each independent variable in the prediction of the dependent variable (i.e. $f\text{CO}_2\text{sw}$).

We found strong relationships (r^2 of 0.79 and β of 0.9) between $f\text{CO}_2\text{sw}$ and $\text{chl a}^{\text{in situ}}$, as well as between $f\text{CO}_2\text{sw}$ and $\text{PP}^{\text{satEpp}}$ (Table 3). This suggests that biological processes explain large parts of the $f\text{CO}_2\text{sw}$ variability in our study. Rangama et al. (2005) also found a strong biological influence on the $f\text{CO}_2\text{sw}$ in a region further north. The $\text{SST}^{\text{in situ}}$ showed weak r^2 (< 0.01) although the β coefficient was moderate (0.09). Another evaluation method for predictive power is to use the residuals (observed–predicted) in a set of step-wise equations to analyze the individual contribution of each predictor variable. For example, the residuals from the single regression $f\text{CO}_2\text{sw} = 354.5616 + 0.9821 \times \text{SST}^{\text{in situ}}$, showed a correlation (r) of 0.18 with quadratic $\text{SST}^{\text{in situ}}$ values (SST^2 in situ). The positive residuals indicated that the predicted $f\text{CO}_2\text{sw}$ was lower than the observed $f\text{CO}_2\text{sw}$. Next, we studied the residuals when the quadratic function of $\text{SST}^{\text{in situ}}$ (SST^2 in situ) was included in the algorithm ($f\text{CO}_2\text{sw} = 342.9543 - 8.465 \times \text{SST} + 2.4745 \times \text{SST}^2$ in situ). In this case the residuals showed no bias with SST or SST^2 in situ ($r = 1 \times 10^{-7}$), meaning that SST^2 in situ adds predictive power to the $f\text{CO}_2\text{sw}$ fit, and the r^2 improved from < 0.01 to 0.13. The improvement by a second term was also found in the regression between $f\text{CO}_2\text{sw}$ and chl a. The residuals from this function showed a negative correlation ($r = -0.26$) meaning that the predicted $f\text{CO}_2\text{sw}$ was too high relative to the in-situ $f\text{CO}_2\text{sw}$. By including $\ln \text{chl a}$ in the fit, the residuals showed insignificant bias ($r = 1 \times 10^{-8}$). Single regression between $f\text{CO}_2\text{sw}$ and PP^{sat} showed lower prediction capability than chl a and $\ln \text{chl a}$, respectively. The residual analysis did not reveal a significant addition to the prediction of $f\text{CO}_2\text{sw}$ ($r < 0.01$, residuals versus $\text{PP}^{\text{satEpp}}$). This implied that VGPM did not add additional information to the effect of biological processes on the variability of $f\text{CO}_2\text{sw}$, and were excluded in our further evaluation

Table 3

Single regression diagnostics for the type of equation: $f\text{CO}_2\text{sw} = kx + m$, where x denotes either of the variables: $\text{SST}^{\text{in situ}}$, $\text{chl a}^{\text{in situ}}$, $\text{PP}^{\text{satEpp}}$, and MLD.

Variable (x)	k	m	r^2	β
$\text{SST}^{\text{in situ}}$	1.064	394.9695	0.007	0.09
SST^2 in situ	0.6998	350.9468	0.059	0.22
$\text{chl a}^{\text{in situ}}$	18.5155	370.4756	0.792	0.90
$\ln \text{chl a}^{\text{in situ}}$	27.1275	332.0621	0.665	0.82
$\text{PP}^{\text{satEpp}}$	0.093	381.3324	0.673	0.87
MLD	0.0528	354.3733	0.007	0.03
$\ln \text{MLD}$	2.1323	360.4107	0.003	0.04

of suitable $f\text{CO}_2\text{sw}$ predictors. In the case of MLD, r^2 for MLD and logarithmic MLD ($\ln \text{MLD}$) showed low correlation in combination with the lowest β coefficients (0.03 and 0.04, respectively). Furthermore, the residuals based on each of the independent variables showed little correlation when plotted against MLD and $\ln \text{MLD}$. This may be due to the fact that HYCOM MLD was not representative of our study area ($r^2 = 0.69$), and also because MLD possessed little impact on the $f\text{CO}_2\text{sw}$ during our study period. Barbero et al. (2011), found that the deepest MLD coincided with highest $f\text{CO}_2\text{sw}$ (i.e. total inorganic carbon, C_T) in late winter in the sub-Antarctic zone (SAZ) of the Pacific Ocean (between 40°S and 55°S). Similar to our study, the correlation was weak during summer and variable C_T values were associated with shallow MLD. Moreover, our study was performed in the area south of the SAZ, where the influence of summer ice-melt water likely leads to further stabilization of the surface layer resulting in shallow MLD.

4.2. Multi-Parameter Linear Regression relationships

According to the analysis in Section 3.3, it was evident that SST from HYCOM showed the largest bias to in situ SST and had the potential to introduce large errors to the predicted $f\text{CO}_2\text{sw}$. The single linear regression analysis (Section 4.1) showed that both MLD and PP^{sat} showed small contributions to the prediction of $f\text{CO}_2\text{sw}$. This concludes that we considered the in-situ and remotely sensed SST and chl a data as variables in further analysis. Three sets of combinations were evaluated; 1) the full-field data set ($\text{SST}^{\text{in situ}}$ and $\text{chl a}^{\text{in situ}}$, $N = 9735$) and, 2) field measurements collocated with remotely sensed data. The data set in Eq. (2) were about 700 data-points smaller than the field-data set, since more than 700 data points were excluded when remotely sensed products were not available due to cloud or ice cover ($\text{SST}^{\text{in situ}}$ and $\text{chl a}^{\text{in situ}}$). In Eq. (3) we used the remotely-sensed chl a and SST products (chl^{rmt} and SST^{rmt}). An additional evaluation criteria are used in this section; the Cost function (CF, Holt et al., 2005) given as

$$CF = \frac{1}{n\sigma^2} \sum_{n=1}^N (E-F)^2$$

Where E are the calculated values based on the fit, F is field measurements, σ is the standard deviation of the field measurements, N is the number of measurements. The CF enables the comparison of the accuracy of the estimated variables, and lower values indicate better performance than higher values. The best fits from the three combinations are presented in Eqs. (1) to (3), together with the coefficient of determination (r^2), root mean square error (rms), the Cost Function (CF), and the total number of data points (N):

$$\begin{aligned} f\text{CO}_2\text{sw} = & 355.3001(\pm 0.3156) - 3.1895(\pm 0.1282) \\ & \times \text{SST}^{\text{insitu}} + 0.8959(\pm 0.0303) \\ & \times (\text{SST}^{\text{insitu}})^2 - 13.7579(\pm 0.1364) \times \text{chl}^{\text{insitu}} - 8.1605(\pm 0.2264) \\ & \times \ln \text{chl}^{\text{insitu}} \quad r^2 = 0.837, \text{rms} = \pm 13.2 \mu\text{atm}, \text{CF} = 0.16, N = 9735 \end{aligned} \quad (1)$$

$$\begin{aligned} f\text{CO}_2\text{sw} = & 355.5750(\pm 0.3370) - 3.1088(\pm 0.1322) \\ & \times \text{SST}^{\text{insitu}} + 0.8687(\pm 0.0310) \times (\text{SST}^{\text{insitu}})^2 \\ & - 13.5593(\pm 0.1522) \times \text{chl}^{\text{insitu}} - 8.1740(\pm 0.2420) \times \ln \text{chl}^{\text{insitu}} \\ r^2 = & 0.818, \text{rms} = \pm 13.6 \mu\text{atm}, \text{CF} = 0.18, N = 8970 \end{aligned} \quad (2)$$

$$\begin{aligned} f\text{CO}_2\text{sw} = & 353.6715(\pm 0.3264) - 2.5417(\pm 0.1509) \\ & \times \text{SST}^{\text{rmt}} + 0.7291(\pm 0.0337) \times (\text{SST}^{\text{rmt}})^2 - 11.5646(\pm 0.1361) \\ & \times \text{chl}^{\text{rmt}} - 10.0477(\pm 0.2418) \times \ln \text{chl}^{\text{rmt}} \end{aligned} \quad (3)$$

$$r^2 = 0.815, \text{rms} = \pm 14.1 \mu\text{atm}, \text{CF} = 0.19, N = 8970$$

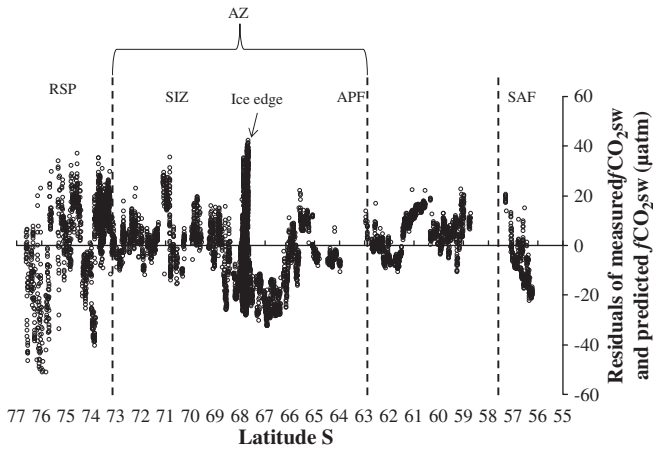


Fig. 7. Residuals (measured-predicted $f\text{CO}_{2\text{sw}}$, μatm) from Eq. (3) are plotted versus latitude south (S). Major fronts and zones are marked. Note that the furthest south is to the left at the axis.

Little difference was seen in the statistical analysis between the three equations. The full in-situ data set (Eq. 1) resulted in a slightly lower CF, better fit based on r^2 of 0.84 and rms of $\pm 13 \mu\text{atm}$ compared to Eqs. (2) and (3). The strong chl a contribution was similar in all three equations, and r^2 greatly improved from 0.13 (using only SST and SST^2) to r^2 of 0.82, using SST, SST^2 and chl a. Moreover, the rms decreased from $\pm 29 \mu\text{atm}$ to $\pm 14 \mu\text{atm}$ using SST, SST^2 and chl a.

We used the variance inflation factors ($\text{VIF} = 1/(1-r^2_i)$) for collinearity diagnostics to check for unwanted cross-correlation between

the independent variables. $\text{VIF} > 5$ indicates the presence of cross-correlation between independent parameters (Belsley et al., 1980). Our approach resulted in VIF for SST, SST^2 , chl a, and $\ln \text{chl a}$ of 4.8, 5.0, 2.6, 2.8, respectively, indicating that our variables did not cross-correlate significantly.

4.3. Comparison between measured and predicted $f\text{CO}_{2\text{sw}}$

The predictive power was further examined using the residuals between the $f\text{CO}_{2\text{sw}}$ measured in the field and the calculated $f\text{CO}_{2\text{sw}}$ from all three equations. In Fig. 7, the residuals from in-situ and calculated $f\text{CO}_{2\text{sw}}$ based on Eq. (3) are shown. Similar patterns were seen in Eqs. (1) and (2) (not shown). Positive residuals indicate that the predicted $f\text{CO}_{2\text{sw}}$ values were too low relative to the measured. The residuals were similar in all three algorithms, which indicated that both field and remotely sensed products have limitations, and did not give a realistic representation of the summer situation. The largest residuals (approximately $\pm 50 \mu\text{atm}$, Fig. 7) were found in the RSP (73°S to 77°S) and at the ice edge (68°S). Given that chl a showed significant influence on the predicted $f\text{CO}_{2\text{sw}}$, we would expect the largest residuals in areas with large chl a bias between the measured and the remotely sensed product. This was the case at the ice edge (Fig. 6a) and in the RSP between 75°S and south of 76.5°S (Fig. 6c).

4.4. Creation of $f\text{CO}_{2\text{sw}}$ maps from the algorithm based on remotely sensed data

We created October to December mean values of chl^{rmt} and SST^{rmt} in grids of $1^\circ \times 1^\circ$ by merging the 8-day MODIS-SeaWiFS 9 km chl a

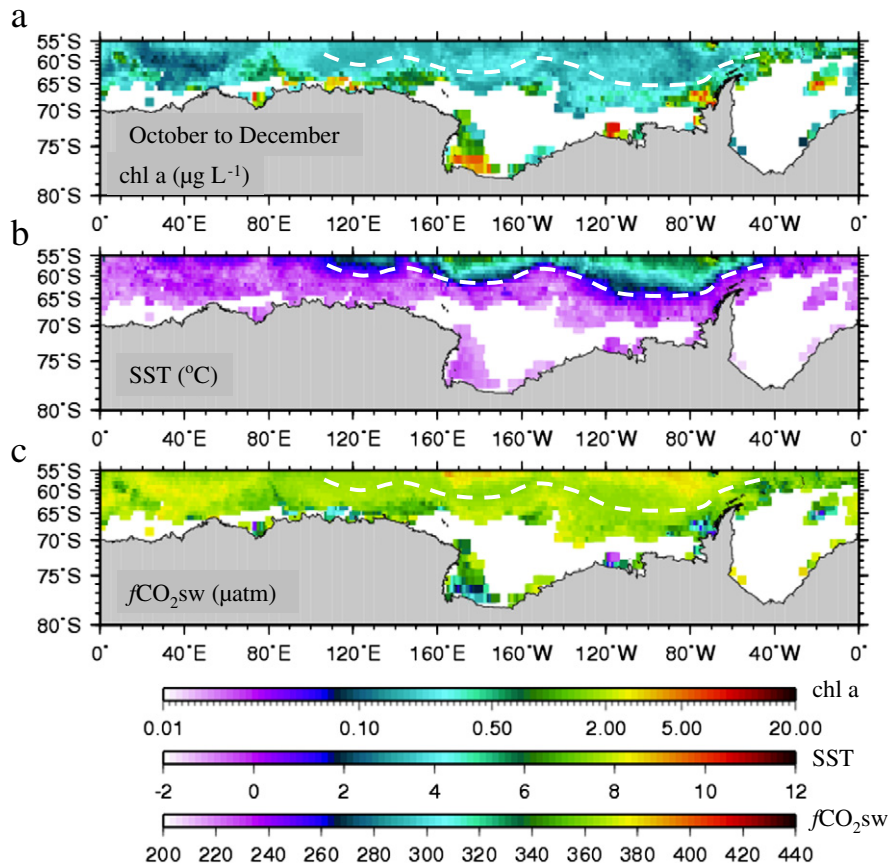


Fig. 8. Mean values from October to December 2006 in a $1^\circ \times 1^\circ$ grid for the circumpolar high latitude sector of the Southern Ocean (179.5°E to 179.5°W, and 55°S to 80°S of: a) remotely sensed chl a ($\mu\text{g L}^{-1}$); b) SST^{rmt} ($^\circ\text{C}$), and c) the computed $f\text{CO}_{2\text{sw}}$ (μatm) from Eq. (3) in this study. The white dashed line indicates the approximate location of the Antarctic Polar Front (APF) based on the SST^{rmt} .

and MODIS Aqua SST data for 2006. We computed the $1^\circ \times 1^\circ$ averages from 179.5°E to 179.5°W and between latitude 54.5°S and 80.5°S . The October to December mean values of chl^{rmt} (Fig. 8a) and SST^{rmt} (Fig. 8b) in each grid were used to calculate the mean $f\text{CO}_{2\text{sw}}$ for October to December 2006 based on Eq (3) (Fig. 8c). Large areas were near the atmospheric CO_2 ($f\text{CO}_{2\text{air}}$) level of $376 \mu\text{atm}$ (GLOBALVIEW-CO₂). In the warm POOZ region, between 55°S and 60°S and 160°E and 80°W , the $f\text{CO}_{2\text{sw}}$ was slightly supersaturated relative to the atmospheric level (Fig. 8c). In this region, the mean chl a levels were low and SST relatively high, indicating that SST may be the major control on $f\text{CO}_{2\text{sw}}$. In a large area, south of the polar front, $f\text{CO}_{2\text{sw}}$ was between 340 and $360 \mu\text{atm}$ and undersaturated by $10 \mu\text{atm}$ to $20 \mu\text{atm}$ relative to the $f\text{CO}_{2\text{air}}$ level suggesting that this area was a summertime atmospheric CO_2 sink. The lowest $f\text{CO}_{2\text{sw}}$ values of approximately $100 \mu\text{atm}$ to $200 \mu\text{atm}$ below $f\text{CO}_{2\text{air}}$ were found in the RSP, and along the West Antarctic Peninsula (WAP). These areas showed high chl a, implying that biological processes play a major role in explaining the $f\text{CO}_{2\text{sw}}$ change in these areas, which agrees with the study of Rangama et al. (2005).

4.5. Validation of the $f\text{CO}_{2\text{sw}}$ algorithm with $f\text{CO}_{2\text{sw}}$ climatology on a seasonal time scale

The limitations of the spatial and seasonal robustness of the algorithm were investigated by comparing the calculated $f\text{CO}_{2\text{sw}}$ values with the $f\text{CO}_{2\text{sw}}$ climatology data set (Takahashi et al., 2009). This enabled a check of the applicability of the algorithm to other regions and at other times, or whether it was strictly valid to the area where data originated. We created mean values for chl^{rmt} and SST^{rmt} for four periods, and binned at a $1^\circ \times 1^\circ$, and calculated $f\text{CO}_{2\text{sw}}$ values from the algorithm (Eq. 3). The climatology data was corrected to the reference year 2006 using the atmospheric $f\text{CO}_{2\text{air}}$ growth function estimated to $1.588 \mu\text{atm year}^{-1}$ based on the GLOBALVIEW CO_2 from Halley Station, Antarctica (75.58°S , 26.5°W , GLOBALVIEW-CO₂, 2009). This data set is hereafter denoted $T_{\text{ref}}2006$ data. The four periods were divided into the following months: 1) January–March, 2) April to June, 3) July to September, and 4) October to December. The seasonal map based on the calculated $f\text{CO}_{2\text{sw}}$ is shown in Fig. 9a, and the seasonal $f\text{CO}_{2\text{sw}}$ from $T_{\text{ref}}2006$ are shown in Fig. 9b. The white areas in

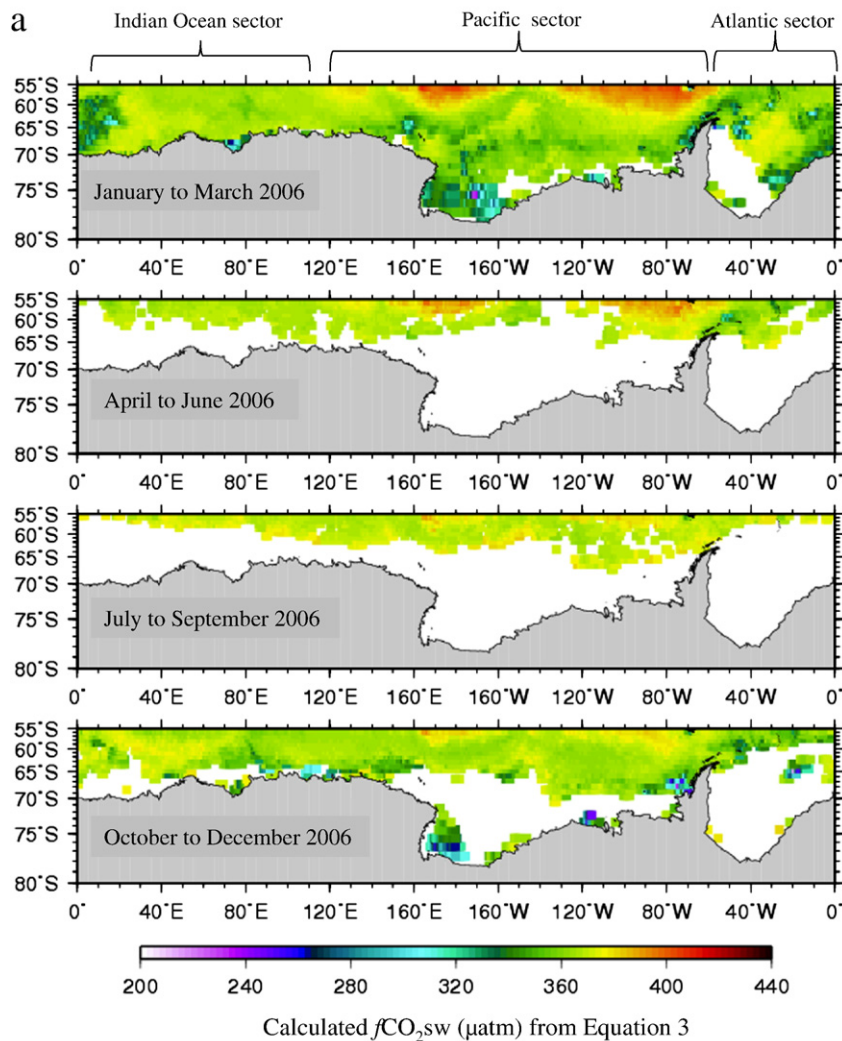


Fig. 9. The $f\text{CO}_{2\text{sw}}$ values in four periods based on: a) calculated $f\text{CO}_{2\text{sw}}$ (μatm) based on Eq. (3) and seasonal mean values of chl^{rmt} and SST^{rmt} , and b) the $f\text{CO}_{2\text{sw}}$ (μatm) included in the climatology data (Takahashi et al., 2009) corrected to the reference year 2006 ($T_{\text{ref}}2006$). From top: January to March; April to June, July to September, and October to December (bottom panel).

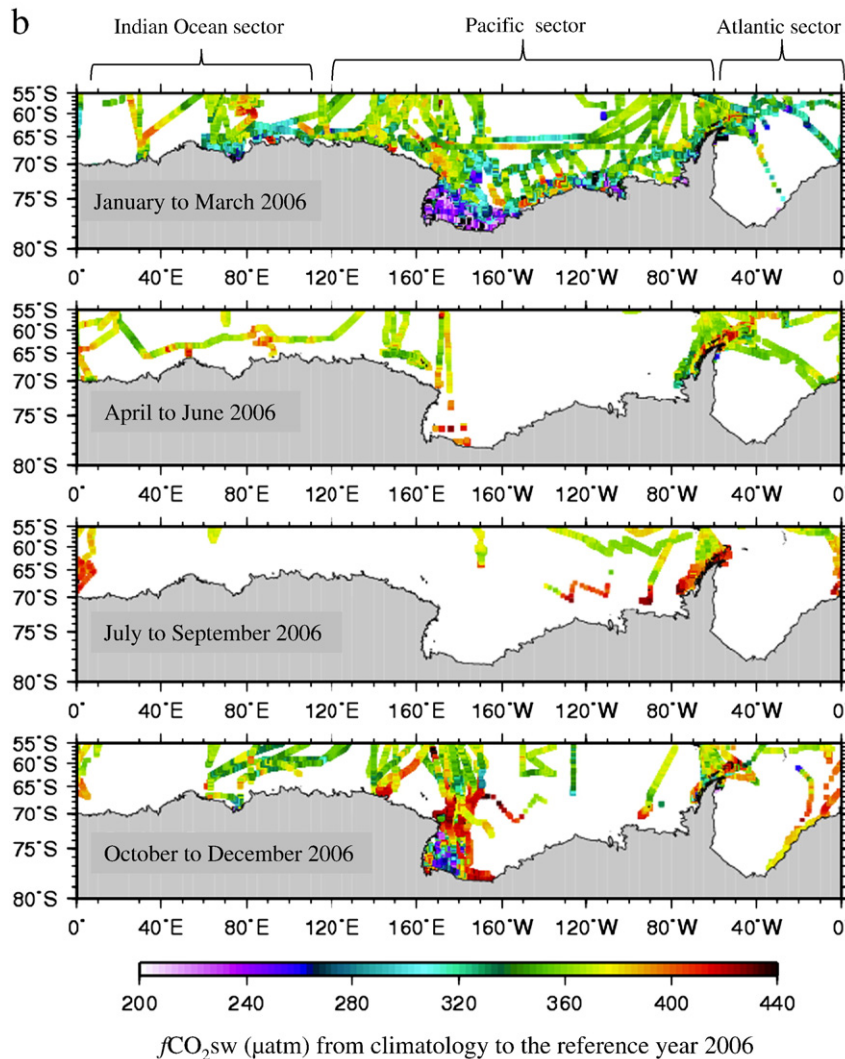


Fig. 9 (continued).

Fig. 9 are locations with sea-ice cover or no data. The Pacific sector north of 60°S (170°E to 100°W), was supersaturated in $f\text{CO}_{2\text{sw}}$ relative to the atmospheric CO_2 level of 390 ppm throughout the year, particularly evident in January to March (Fig. 9a). This area in the POOZ had the warmest SST and lowest chl a (Fig. 8, for Oct–Dec). This implies that SST was the main driver on the seasonal $f\text{CO}_{2\text{sw}}$ and that biological processes play a minor role in this part of the Pacific sector. In the southern Pacific sector and in the Indian Ocean sector, the $f\text{CO}_{2\text{sw}}$ was generally close to or undersaturated relative to the atmospheric CO_2 level for the whole year. In the southern Western Antarctic Peninsula (WAP), the Amundsen Sea, the Ross Sea, and the Prydz Bay (~80°E), the $f\text{CO}_{2\text{sw}}$ decreased at the onset of sea-ice retreat in October to December (Fig. 9a). In January to March, $f\text{CO}_{2\text{sw}}$ was at a minimum in these regions, which may be due to biological CO_2 uptake during biological primary production as a consequence of the opening of coastal polynyas. In these areas, the climatology showed similar seasonal cycle, but with lower $f\text{CO}_{2\text{sw}}$ values in January to March than the calculated $f\text{CO}_{2\text{sw}}$ data. This implies that the algorithm captured the seasonal $f\text{CO}_{2\text{sw}}$ trend relatively well in these areas.

The high calculated $f\text{CO}_{2\text{sw}}$ in the Pacific sector of the POOZ in January to March (170°E to 100°W, Fig. 9a, top panel) were not detected in the climatology data (Fig. 9b, top panel). One possible explanation is that the SST^{mtc} data used in the algorithm was unrealistically high, which resulted in biased $f\text{CO}_{2\text{sw}}$ values. The $T_{\text{ref}2006}$

data showed the lowest $f\text{CO}_{2\text{sw}}$ values in January to March, which agrees with the timing of maximum phytoplankton production (Arrigo et al., 1998). The high climatological $f\text{CO}_{2\text{sw}}$ values close to the WAP (Fig. 9b) in the fall were likely due to physical mixing of CO_2 -rich subsurface water, which was not found in the calculated $f\text{CO}_{2\text{sw}}$.

5. Summary

We predicted the $f\text{CO}_{2\text{sw}}$ to a standard error within 14 µatm for December 2006 in the high-latitude Pacific sector of the Southern Ocean. The full in-situ data set resulted in a slightly improved fit ($r^2 = 0.84$ and $\text{rms} = \pm 13$ µatm) relative to the algorithm derived from remotely-sensed data. This may be due to the better representation of areas with large bias between in-situ and satellite products such as at the ice edge. However, the relatively small difference between the r^2 and rms of the three algorithms are probably because our data set was limited to December and did not capture the full CO_2 -system dynamics. It is likely that physical processes such as changes in the mixed layer depth have had larger influence on the surface $f\text{CO}_{2\text{sw}}$ during spring and fall than that from biological processes. The largest bias between in-situ SST and chl a data was observed in areas with large variability such as at the ice edge, in the Polar Front region, and in the Ross Sea Polynya. Clearly, the satellite chl a product could not resolve the localized areas of high chl a

values, associated with fronts and the sea-ice edge at the spatial and temporal resolutions that are available in this area. This implies the need for both technical developments for increased sensitivity and refinement of the algorithms used to be able to improve estimates and understanding of the biogeochemical processes behind the variability of CO₂ in the surface water. Efforts should concern the development and optimization of remote-sensing capabilities both on the regional and global scale. We believe that the use of field measurements with seasonal coverage together with remotely sensed products and ocean data model products to create *f*CO_{2sw} algorithms greatly improve the oceanic CO₂ uptake estimates for the relatively unexplored Southern Ocean.

Acknowledgments

This is a contribution to the Remote Sensing Carbon UptakeE, RESCUE, (Dnrs: 96/05 and 100/09) projects funded by the Swedish National Space Board, CARBON-HEAT (185093/S30) of the Norwegian Research Council, Swedish Research Council (2009–2994), The Swedish Research Council Formas, and the EU IP CARBOOCEAN (GOCE511176-2). We are grateful to the NASA Ocean Biology and Biogeochemistry Program for the support provided to one of the collaborators in this project (Sergio Signorini). We thank the three reviewers for constructive comments and recommendations that significantly improved the manuscript.

We are also grateful for the excellent support given by the Captain and crew onboard the IB Oden. We thank the Swedish Polar Research Secretariat, and the US National Science Foundation for preparative and logistical support for the Oden Southern Ocean expedition in 2006.

References

- Allen, J. I., Holt, J. T., Blackford, J., & Proctor, R. (2007). Error quantification of a high-resolution coupled hydrodynamic ecosystem coastal-ocean model: Part 2. Chlorophyll-*a*, nutrients and SPM. *Journal of Marine Systems*, 68, 381–404.
- Arrigo, K. R., Schnell, A., Worthen, D. L., & Lizotte, M. P. (1998). Primary production in Southern Ocean waters. *Journal of Geophysical Research*, 103, 15587–15600.
- Arrigo, K. R., & Van Dijken, G. L. (2003). Phytoplankton dynamics within 37 Antarctic coastal polynya systems. *Journal of Geophysical Research*, 108(No. C8), 3271, doi: 10.1029/2002JC001739.
- Arrigo, K. R., & Van Dijken, G. L. (2007). Interannual variation in air–sea CO₂ flux in the Ross Sea, Antarctica: A model analysis. *Journal of Geophysical Research*, 112, C03020, doi:10.1029/2006JC003492.
- Bakker, D. C. E., de Baar, H. J. W., & Bathmann, U. V. (1997). Changes of carbon dioxide in surface-waters during spring in the Southern Ocean. *Deep Sea Research II*, 44, 91–128.
- Bakker, D. C. E., Hoppema, M., Schröder, M., Geibert, W., & de Baar, H. J. W. (2008). A rapid transition from ice covered CO₂-rich waters to a biologically mediated CO₂ sink in the eastern Weddell Gyre. *Biogeosciences*, 5, 1373–1386 www.biogeosciences.net/5/1373/2008/
- Barbero, L., Boutin, J., Merlivat, L., Martin, N., Takahashi, T., Sutherland, S. C., et al. (2011). Importance of water mass formation regions for the air–sea CO₂ flux estimate in the Southern Ocean. *Global Biogeochemical Cycles*, 25, GB1005, doi: 10.1029/2010GB003818.
- Beer, T. (1983). Environmental oceanography. *Textbook to "The applied Environmental Oceanographical Tables"* (pp. 117–129). Oxford: Pergamon Press.
- Behrenfeld, M. J., & Falkowski, P. G. (1997). Photosynthetic rates derived from satellite-based chlorophyll concentration. *Limnology and Oceanography*, 42(1), 1–20.
- Belsley, D. A., Kuh, E., & Welsch, R. E. (1980). *Regression diagnostics: Identifying influential data and sources of collinearity*. New York: Wiley.
- Boutin, J., Etcheto, J., Dandonneau, Y., Bakker, D. C. E., Feely, R. A., Inoue, H. Y., et al. (1999). Satellite sea surface temperature: A powerful tool for interpreting in situ pCO₂ measurements in the equatorial Pacific Ocean. *Tellus*, 51B, 490–508.
- Chierici, M., & Fransson, A. (2009). CaCO₃ saturation in the surface water of the Arctic Ocean: Undersaturation in freshwater influenced shelves. *Biogeosciences*, 6, 2421–2432 www.biogeosciences.net/6/2421/2009/
- Chierici, M., Fransson, A., Turner, D., Pakhomov, E. A., & Froneman, P. W. (2004). Variability in pH, *f*CO₂, oxygen and flux of CO₂ in the surface water along a transect in the Atlantic sector of the Southern Ocean. *Deep Sea Research II*, 51, 2773–2787, doi: 10.1016/j.dsr2.2001.03.002.
- Chierici, M., Olsen, A., Trinañes, J., Wanninkhof, R., & Johannessen, T. (2009). Algorithms to estimate carbon dioxide in the upper subarctic North Atlantic using observations, modeled mixed layer depth and remotely derived chlorophyll. *Deep Sea Research II*, doi:10.1016/j.dsr2.2008.12.014.
- Dickson, A. G. (1990). Standard potential of the (AgCl(s) + 1/2H₂(g) = Ag(s) + HCl(aq)) cell and the dissociation constant of bisulfate ion in synthetic sea water from 273.15 to 318.15 K. *The Journal of Chemical Thermodynamics*, 22, 113–127.
- Dickson, A. G., Sabine, C. L., & Christian, J. R. (Eds.). (2007). *Guide to best practices for ocean CO₂ measurements*. PICES Special Publication, 3, .
- Eppley, R. W. (1972). Temperature and phytoplankton growth in the sea. *Fisheries Bulletin*, 70, 1063–1085.
- GLOBALVIEW-CO₂: Cooperative Atmospheric Data Integration Project - Carbon Dioxide. CD-ROM, NOAA ESRL, Boulder, Colorado [Also available on Internet via anonymous FTP to ftp.cmdl.noaa.gov, Path: cgg/co2/GLOBALVIEW], 2009.
- Haraldsson, C., Anderson, L. G., Hasselöv, M., Hulth, S., & Olsson, K. (1997). Rapid, high-precision potentiometric titration of alkalinity in the ocean and sediment pore waters. *Deep Sea Research I*, 44, 2031–2044.
- Harashima, A., Tsuda, R., Tanaka, Y., Kimoto, T., Tatsuta, H., & Furusawa, K. (1997). Monitoring algal blooms and related biogeochemical changes with a flow-through system deployed on ferries in the adjacent seas of Japan. In M. Kahru, & C. Brown (Eds.), *Monitoring Algal Blooms: New Techniques for Detecting Large-Scale Environmental Change* (pp. 85–112). : Springer-Verlag.
- Holm-Hansen, O., & Riemann, B. (1978). Chlorophyll-*a* determination: Improvements in methodology. *Oikos*, 30, 438–447.
- Holt, J. T., Allen, J. I., Proctor, R., & Gilbert, F. (2005). Error quantification of a high-resolution coupled hydrodynamic ecosystem coastal-ocean model: Part 1. model overview and assessment of the hydrodynamics. *Journal of Marine Systems*, 57, 167–188.
- Hoppema, M., Stoll, M. H. C., & De Baar, H. J. W. (2000). CO₂ in the Weddell Gyre and Antarctic Circumpolar Current: Austral autumn and early winter. *Marine Chemistry*, 72, 203–220.
- Hurlburt, H. E., Brassington, G. B., Drillet, Y., Kamamachi, M., Benkiran, M., Bourdallé-Badie, R., et al. (2009). High-resolution global and basin-scale ocean analyses and forecasts. *Oceanography*, 22(3), 110–127.
- Inoue-Yoshikawa, H., & Ishii, M. (2005). Variations and trends of CO₂ in the surface seawater in the Southern Ocean south of Australia between 1969 and 2002. *Tellus*, 57B, 58–69.
- Kimoto, T., & Harashima, A. (1993). High resolution time/space monitoring of the surface seawater CO₂ partial pressure by ship-of-opportunity. *Fourth International Carbon Dioxide Conference Abstracts* (pp. 88–91). France: Carqueiranne.
- Le Quéré, C., Rödenbeck, C., Buitenhuis, E. T., Conway, T. J., Langenfelds, R., Gomez, A., et al. (2007). Saturation of the Southern ocean CO₂ sink due to recent climate change. *Science*, 316, 1735–1738.
- Lorbacher, K., Dommenges, D., Niiler, P. P., & Köhl, A. (2006). Ocean MLD: A subsurface proxy of ocean atmosphere variability. *Journal of Geophysical Research*, 111, 22, doi: 10.1029/2003JC002157.
- McNeil, B. I., Metzl, N., Key, R. M., Matar, R. J., & Corbiere, A. (2007). An empirical estimate of the Southern Ocean air–sea CO₂ flux. *Global Biogeochemical Cycles*, 21, GB3011, doi:10.1029/2007GB002991.
- Metzl, N. (2009). Decadal increase of organic carbon dioxide in Southern Indian Ocean surface waters (1991–2007). *Deep Sea Research II*, 56, 607–619.
- Metzl, N., Tilbrook, B., & Poisson, A. (1999). The annual *f*CO₂ cycle and the air–sea CO₂ flux in the sub-Antarctic Ocean. *Tellus*, 51B, 849–861.
- Moore, K. J., & Abbott, M. R. (2000). Phytoplankton chlorophyll distributions and primary production in the Southern Ocean. *Journal of Geophysical Research*, 105 (C12), 28709–28722.
- Morel, A. (1991). Light and marine photosynthesis: A spectral model with geochemical and climatological implications. *Progress in Oceanography*, 26, 263–306.
- Nondal, G., Bellerby, R. G. J., Olsen, A., Johannessen, T., & Olafsson, J. (2009). Optimal evaluation of the surface ocean CO₂ system in the northern North Atlantic using data from voluntary observing ships. *Limnology and Oceanography Methods*, 7, 109–118.
- Olsen, A., Brown, K. M., Chierici, M., Johannessen, T., & Neill, C. (2008). Sea surface CO₂ fugacity in the subpolar North Atlantic. *Biogeosciences*, 5, 535–547.
- Olsen, A., Trinañes, J. A., & Wanninkhof, R. (2004). Sea-air flux of CO₂ in the Caribbean Sea estimated using in situ and remote sensing data. *Remote Sensing of Environment*, 89, 309–325.
- Orsi, A. H., & Whitworth, T., III (2005). Hydrographic Atlas of the World Ocean Circulation Experiment (WOCE). In M. Sparrow, P. Chapman, & J. Gould (Eds.), *International WOCE Project Office. Southern Ocean, Volume 1*, Southampton, UK.
- Orsi, A. H., Whitworth, T., III, & Worth, D. N., Jr. (1995). On the meridional extent and fronts of the Antarctic Circumpolar Current. *Deep Sea Research I*, 42, 641–673.
- Ozsoy-Cicek, B., Xie, H., Ackley, S. F., & Ye, K. (2008). Antarctic summer sea ice concentration and extent: Comparison of ODEN 2006 ship observations, satellite passive microwave and NIC sea ice charts. *The Cryosphere Discuss*, 2, 623–647 www.the-cryosphere-discuss.net/2/623/2008/
- Pierrot, D., Lewis, E., & Wallace, D. W. R. (2006). *MS Excel Program developed for CO₂ system calculations, ORNL/CDIAC-105*. Carbon Dioxide Information Analysis Center, Oak Ridge National Laboratory, U.S. Department of Energy, Oak Ridge, Tennessee.
- Poisson, A., Metzl, N., Brunet, C., Schauer, B., Bres, B., Ruiz-Pino, D., & Louchfi, F. (1993). Variability of sources and sinks of CO₂ in the western Indian and Southern Oceans during the year 1991. *Journal of Geophysical Research*, 98, 22,759–22,778.
- Press, W. H., Flannery, B. P., Teukolsky, S. A., & Vetterling, W. T. (1986). *Numerical recipes*. Cambridge, UK: Cambridge University.
- Rangama, Y., Boutin, J., Etcheto, J., Merlivat, L., Takahashi, T., Delille, D., et al. (2005). Variability of the net air–sea CO₂ flux inferred from shipboard and satellite measurements in the Southern Ocean south of Tasmania and New Zealand. *Journal of Geophysical Research*, 110, C09005, doi:10.1029/2004JC002619.
- Robertson, J. E., & Watson, A. J. (1995). A summer time sink for atmospheric CO₂ in the Southern Ocean 88°W and 80°E. *Deep Sea Research II*, 42, 1081–1091.

- Roy, R. N., Roy, L. N., Vogel, K. M., Porter-Moore, C., Pearson, T., Good, C. E., et al. (1993). The dissociation constants of carbonic acid in seawater at salinities 5–45 and temperatures 0–45 °C. *Marine Chemistry*, *44*, 249–267.
- Roy, R. N., Roy, L. N., Vogel, K. M., Porter-Moore, C., Pearson, T., Good, C. E., et al. (1994). Erratum for: The dissociation constants of carbonic acid in seawater at salinities 5–45 and temperatures 0–45 °C. *Marine Chemistry*, *45*, 337.
- Sarmiento, J. L., Hughes, T. M. C., Stouffer, R. J., & Manabe, S. (1998). Simulated response of the ocean carbon cycle to anthropogenic climate warming. *Nature*, *393*, 245–249.
- Stephens, M. P., Samuels, G., Olson, D. B., Fine, R. A., & Takahashi, T. (1995). Sea–air flux of CO₂ in the North Pacific using shipboard and satellite data. *Journal of Geophysical Research*, *100*, 13571–13583.
- Sweeney, C., Hansell, D. A., Carlson, C. A., Codispoti, L. A., Gordon, L. I., Marra, J., et al. (2000). Biogeochemical regimes, net community production and carbon export in the Ross Sea, Antarctica. *Deep Sea Research II*, *47*, 3369–3394.
- Takahashi, T., Olafsson, J., Goddard, J., Chipman, D. W., & Sutherland, S. C. (1993). Seasonal variation of CO₂ and nutrients in the high-latitude surface oceans: A comparative study. *Global Biogeochemical Cycles*, *7*, 843–878.
- Takahashi, T., Sutherland, S. C., Wanninkhof, R., Sweeney, C., Feely, R. A., Chipman, D. W., et al. (2009). Climatological mean and decadal change in surface ocean pCO₂, and net sea–air CO₂ flux over the global oceans. *Deep Sea Research II*, doi: [10.1016/j.dsr2.2008.12.009](https://doi.org/10.1016/j.dsr2.2008.12.009).
- Telzewski, M., Chazottes, A., Schuster, U., Watson, A. J., Moulin, C., Bakker, D. C. E., et al. (2009). Estimating the monthly pCO₂ distribution in the North Atlantic using a self-organizing neural network. *Biogeosciences*, *6*, 1405–1421.
- Weiss, R. F., Jahnke, R. A., & Keeling, C. D. (1982). Seasonal effects of temperature and salinity on the partial pressure of CO₂ in seawater. *Nature*, *300*, 511–513.
- Weiss, R. F., & Price, B. A. (1980). Nitrous oxide solubility in water and seawater. *Marine Chemistry*, *8*, 347–359.